Intrazeolite Anchoring of Ruthenium Carbonyl Clusters: Synthesis, Characterization, and Their Catalytic Performances

James G. C. Shen,*,† An Ming Liu,‡ Toshihiro Tanaka,§ and Masaru Ichikawa§

Lash Miller Chemical Laboratories, Department of Chemistry, University of Toronto, 80 St George Street, Toronto, Ontario, M5S 3H6 Canada; State Key Laboratory of Catalysis, Dalian Institute of Chemical Physics, Chinese Academy of Sciences, Dalian 116023, China; and Catalysis Research Center, Hokkaido University, Sapporo 060, Japan

Received: January 16, 1998; In Final Form: July 23, 1998

This paper focuses attention on the intrazeolite anchoring of ruthenium carbonyl clusters and their catalytic performances. The synthesis involves the adsorption of metal carbonyl species or metal ion exchange into zeolite cages followed by reductive carbonylation under a mixed CO and H_2 atmosphere. The characterization of the structure and properties of these samples was based on a multianalytical approach, including FT-IR, UV−vis, EXAFS spectroscopies, CO/H_2 gas chemisorption, and ^{13}CO isotopic exchange. Methane homologation was carried out on the zeolitic ruthenium clusters using a two-step process. The research encompassed several key points as follows. (i) $[Ru_3(CO)_{12}]$ guests in $Na_{56}Y$ zeolite were thermally activated in a hydrogen atmosphere, generating intrazeolitic $[H_4Ru_4(CO)_{12}]$. (ii) Hexammineruthenium(III) complexes in $Na_{56}X$ zeolite were thermally activated progressively in a mixed CO and H_2 atmosphere. The generation process was considered to occur through conversion of the intermediate $[Ru(NH_3)_5(CO)]^{2+}$ and $Ru^I(CO)_3$ to $[Ru_6(CO)_{18}]^{2-}$. (iii) Internal and external confinements of ruthenium carbonyl clusters were compared. (iv) A rapid $^{13}CO/^{12}CO$ isotopic exchange was found to reversibly occur for $[Ru_6(CO)_{18}]^{2-}/Na_{56}X$ under H_2 coexistence. (v) Oxidation fragmentation under an O_2 atmosphere and reductive regeneration under a mixed CO and H_2 atmosphere were found to reversibly occur for the intrazeolite anchoring of $[Ru_6(CO)_{18}]^{2-}$. (vi) Comparison of the orbitally degenerate ground state for free Ru carbonyl clusters versus the intrazeolitic anchoring site provides a theoretical indication of the symmetry distortion. (vii) Surface carbonaceous fragments were generated by CH_4 dissociation on the activated ruthenium clusters based on the analysis of TPD, FT-IR, and mass spectroscopies. These fragments are the precursors for hydrocarbon formation. (viii) The catalytic properties of the intrazeolitic ruthenium clusters showed cluster size dependence. Basic $Na_{56}X$ is superior to $Na_{56}Y$ in enchancing methane conversion and C_{2+} hydrocarbons selectivity.

Introduction

The smaller the metal particles, the larger the fraction of metal atoms that are exposed at the surface where they are accessible to reactant molecules and available for catalysis.[1,2] However, since the structures of traditional supported metal catalysts typically consist of metal particles distributed over the internal surface of the support,[3,4] and because most supported metal particles are nonuniform in size/shape and too small to be characterized precisely, their structures are not well understood. Moreover, the relationship between surface structure of traditional catalysts, the rate of individual reaction steps, and overall catalytic pathways is not well understood. Supported metal clusters have been developed recently in which the catalyst contains metal almost exclusively in the form of clusters. The synthesis involves organometallic chemistry on the surface, gas-phase cluster chemistry, and novel preparations in zeolite cages. The latter has been rapidly developed during the past decade; for example, intrazeolite anchoring of Co,[5] Ru,[6] Rh,[7] and Ir[8] carbonyl clusters have been prepared by "ship-in-a-bottle" techniques.

This paper focuses on the synthesis of ruthenium carbonyl clusters inside zeolite cages using a gas/solid-state chemical route, rather than synthesis in the organic solvents. A multi-analytical approach, including FT-IR, UV−vis, extended X-ray absorption fine structure (EXAFS) spectroscopies, CO/H_2 chemisorption, and ^{13}CO isotopic exchange, provides a rather direct and informative picture of the formation of ruthenium carbonyl clusters inside $Na_{56}Y/Na_{56}X$ cages. The reductive carbonylation of the $[Ru^{III}(NH_3)_6]$ and $[Ru_3(CO)_{12}]$ within the cavities under a mixed CO and H_2 or under a H_2 atmosphere, models of the intrazeolite anchoring of ruthenium carbonyl clusters, and the orbitally degenerate ground state for free Ru carbonyl clusters vs the intrazeolite anchoring state are also discussed.

Methane homologation is developed in a two-step procedure by thermal dissociation of methane on a supported metal catalyst, followed by hydrogenation of the surface species deposited on the catalyst.[9] The surface adspecies seems to be the key factor for hydrocarbon formation. In this procedure, a high metallic surface area per unit mass is necessary for the chemisorption of methane and subsequent hydrogenation. The well-defined intrazeolite anchoring of ruthenium clusters makes them attractive catalysts due to their large metallic surface area and small particle size in comparison with traditional metal

* To whom correspondence should be addressed. E-mail: jshen@yesic.com.
† University of Toronto.
‡ Chinese Academy of Sciences.
§ Hokkaido University.

S1089-5647(98)00799-8 CCC: $15.00
Published on Web 09/09/1998

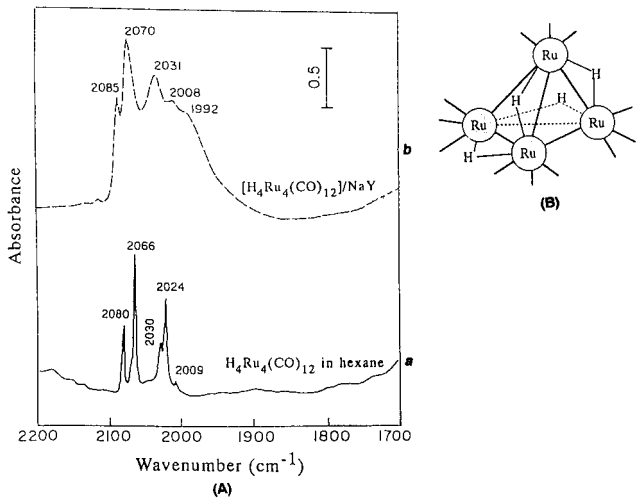

Figure 1. (A) FT-IR spectra obtained for (a) crystalline $H_4Ru_4(CO)_{12}$ in hexane solution and (b) sample *a*. (B) Molecular configuration of crystalline $[H_4Ru_4(CO)_{12}]$.

catalysts. The oxide framework of zeolite is considered to be a macrospheroidal, multisite, multidenate "zeolate" ligand.[10] The combination with metallic clusters is expected to carry great potential. These are expected to favor catalysis behavior in methane homologation. Furthermore, the clusters (metal particles with diameters <10 Å) are considered to be model catalysts, similar to the surface of single-crystal metal. Thus, methane homologation over these clusters reveals relevant details such as reactive intermediates, reaction steps, overall catalytic reaction mechanism, linkages between the reaction rate and the clusters structure, and the host zeolite potential. The latter part of this paper reports the methane homologation on the intrazeolite anchoring of ruthenium clusters including the catalytic activity, selective behavior, reaction intermediates, and reaction mechanism.

Results

Sample Characterization. *Characterization of Sample a.* The IR wafer of $[Ru_3(CO)_{12}]/Na_{56}Y$ is exposed to 400 Torr of H_2. A thermal treatment at room temperature even for 100 h did not produce any significant color change. However, when the temperature was raised to 363 K, a significant vaporization immediately occurred. After 24 h under a H_2 atmosphere, despite differences in the amplitudes of peaks, the IR bands of sample *a* at 2085 (s), 2070 (vs), 2031 (s), 2008 (m), and 1992 cm^{-1} (w) (Figure 1A, line b) resemble those of $[Ru_4H_4(CO)_{12}]$ in hexane at bands of 2080 s, 2066 vs, 2030 m, 2024 s and 2009 w cm^{-1} (Figure 1A, line a, and Table 1).[11] Figure 2 and Table 2 show the diffuse reflectance absorption of the yellow sample *a* at 364 nm, which is analogous to that of the yellow crystal $[H_4Ru_4(CO)_{12}]$ (λ_{max} 360 nm).[12]

IR Characterization of the Generation Process for Sample b. The fresh sample of $[Ru^{III}(NH_3)_6]/NaX$ shows IR bands at 1640 and 1356 cm^{-1} (Figure 3A, line a), which is attributed to υ_2, δ(H−N−H), and υ_4, δ(H−N−H), of ammonia ligand, respectively (where 1640 cm^{-1} is an overlap of H−N−H and H_2O vibration frequencies).[13] On exposing an IR wafer of the fresh sample to CO + H_2 (200 Torr + 200 Torr) in a closed circulating system at 353 K, the IR bands arise at 2072 (w), 2000 (w), and 1939 cm^{-1} (m) (Figure 3A, line b), with the latter predominant band assigned to $[Ru^{II}(NH_3)_5(CO)]$ species. Simultaneously, the original band at 1356 cm^{-1} shifts to 1331 cm^{-1} with diminution in intensity, and a new band appears at

TABLE 1: Carbonyl Stretching Frequencies (ν_{CO}, cm^{-1}) and Assignment for Crystalline $[H_4Ru_4(CO)_{12}]$ and $[H_4Ru_4(CO)_{12}]/Na_{56}Y$

$H_4Ru_4(CO)_{12}$		$H_4Ru_4(CO)_{12}/Na_{56}Y$
IR	Raman[a]	IR
	2019 (s)	
2080 (s)	2078 (w)	2085 (s)
2066 (vs)	2061 (w)	2070 (vs)
2030 (m)	2030 (m)	2031 (s)
2024 (s)	2021 (s)	2008 (m)
2009 (w)	2014 (s)	1992 (w)
	2010 (s)	
	2002 (m)	
	1990 (m)	
	1585 (w)	
	1290 (w)	

[a] Reference 11b.

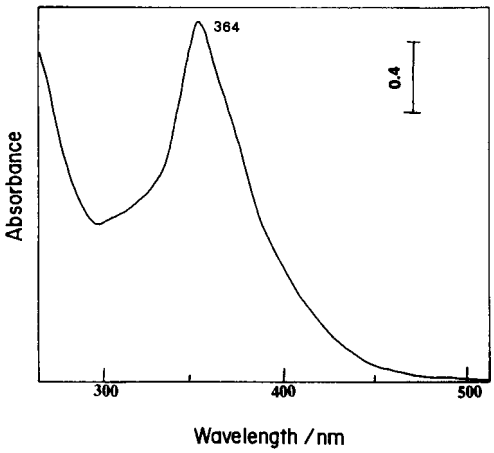

Figure 2. Diffuse reflectance spectra obtained for synthetic sample *a*.

TABLE 2: Electronic Absorption Band Maxima of Ruthenium Carbonyl Clusters. Dependence on Metal−Metal Bond Strength

sample	λ_{max}/nm	assignment
$H_4Ru_4(CO)_{12}$[a]	360	$\sigma^{*\prime} \rightarrow \sigma^*$
$H_4Ru_4(CO)_{12}/NaY$	364	$\sigma^{*\prime} \rightarrow \sigma^*$
$[PPN]_2[Ru_6(CO)_{18}]$	285	
	235	
$[Ru_6(CO)_{18}/NaX$	287	
	235	

[a] Reference 12.

1468 cm^{-1}, attributed to υ_4, δ(N−H), of NH_4^+. This change in the IR spectrum of the N−H vibrations is typical upon reduction of Ru^{III} in zeolite.[14] When the temperature was raised to 393 K, the IR spectrum shows peaks at 2088, 2048, 2014, and 1952 cm^{-1} (Figure 3A, line c). The bands at 2088 and 2014 cm^{-1} are ascribed to $Ru^I(CO)_2$, and the bands at 2048 and 1952 cm^{-1} are ascribed to $Ru^I(CO)_3$ species (Table 3).[14b] In addition to carbonyl bands, an unidentified peak emerges at low wavenumber (862 cm^{-1}), probably associated with the interaction of mononuclear ruthenium carbonyl species with oxygen of the zeolite framework.[15,16] After 22 h at 393 K, a steady-state spectrum (Figure 3A, line d) is observed, exhibiting carbonyl bands at 2000 (s), 1970 (vs), 1925 (m), and 1747 cm^{-1} (w), while the band at 862 cm^{-1} disappeared. The resulting bands of sample *b* closely resemble those of $[N(PPh_3)_2]_2[Ru_6(CO)_{18}]$ in dichloromethane [υ_{CO}: 2006 (s), 1986 (vs), 1930 (m), and 1754 cm^{-1} (w)][17] (Figure 3B,C), but with shifting of the carbonyl band to lower frequency.

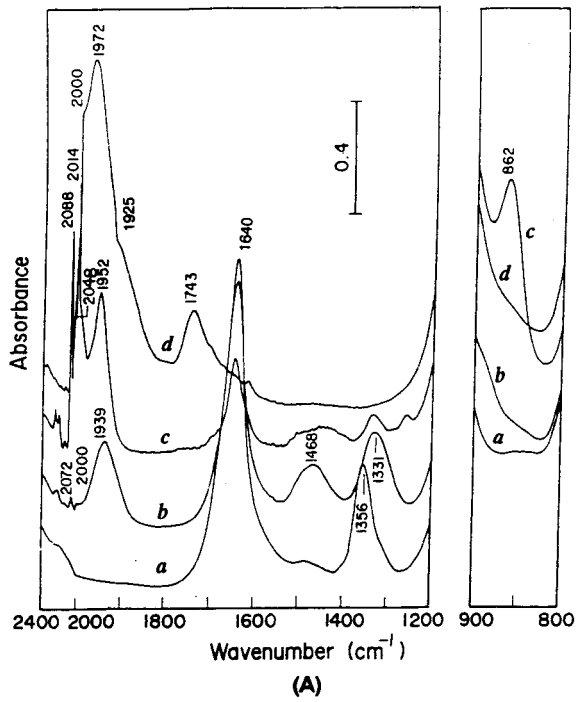

Figure 3. (A) In situ FT-IR spectra in the reaction of $[Ru^{III}(NH_3)_6]/Na_{56}X$ with CO and H_2 (200 and 200 Torr) at 298−393 K: (a) initial spectrum in vacuo, 298 K; (b) 353 K; (c) 393 K, 30 min; (d) 393 K, 22 h. (B) FT-IR spectra obtained for crystalline $[Ru_6(CO)_{18}]^{2-}$ in dichloromethane solution. (C) Molecular configuration of crystalline $[Ru_6(CO)_{18}]^{2-}$.

TABLE 3: Carbonyl Stretching Frequencies (ν_{CO}, cm^{-1}) and Assignment for Crystalline $[Ru_6(CO)_{18}]^{2-}$ and $[Ru_6(CO)_{18}]^{2-}/Na_{56}X$, $Ru^I(CO)_2/Na_{56}X$, and $Ru^I(CO)_3/Na_{56}X$

$[Ru_6(CO)_{18}]^{2-}$ [a]	$[Ru_6(CO)_{18}]^{2-}/Na_{56}X$	$Ru^I(CO)_2/Na_{56}X$	$Ru^I(CO)_3/Na_{56}X$
2006 (s)	2000 (s)	2088 (s)	2048 (s)
1986 (vs)	1972 (vs)	2014 (m)	1952 (m)
1930 (m)	1925 (m)		
1754 (w)	1747 (w)		

[a] Reference 17.

Diffuse Reflectance Characterization of the Generation Process for Sample b. Figure 4 shows the in situ reflectance spectra of the reaction of $[Ru^{III}(NH_3)_6]/Na_{56}Y$ under CO (200 Torr) and H_2 (200 Torr) atmosphere. The parent sample shows four absorption bands at 285, 380, 555, and 750 nm (Figure 4, line a), the 555 nm band of which is close to Ru-red.[18] The band distribution caused from the hexaamine ligands is unstable in $Na_{56}X$ zeolite and is easily converted to Ru-red or Ru-brown having wine-red color.[14b] After 20 h at 343 K under a mixed CO and H_2 atmosphere, the diffuse reflectance spectrum is transformed into an absorption curve with bands at 235, 280, 390, and 550 nm (Figure 4, line b), and the sample appears light yellow. As the temperature reached 373 K for 46 h, two new absorption bands at 240 and 340 nm are observed (Figure 4, line c). Unfortunately, it is difficult to assign in detail these two bands at present. However, in comparison with the IR spectrum of the relative sample, such bands are associated with the formation of mononuclear ruthenium carbonyl species in $Na_{56}X$ zeolite. After the sample was heated for 22 h at 393 K, the new bands emerge at 235 and 287 nm (Figure 4, line d, and Table 2). The reflectance spectrum of the resulting sample *b* at 235 and 287 nm closely resembles those of crystalline $[PPN]_2[Ru_6(CO)_{18}]$ in tetrahydrofuran (THF) solution (λ_{max}: 235 and 285 nm in Table 2).

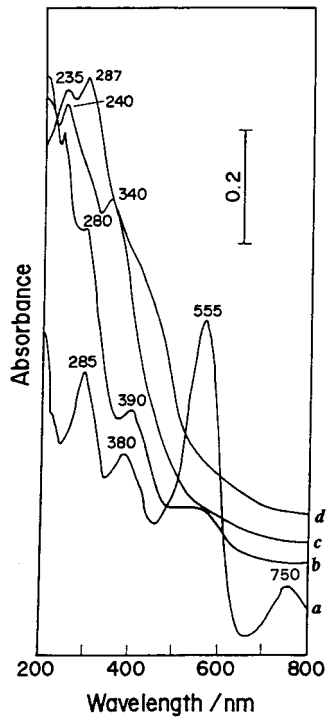

Figure 4. In situ diffuse reflectance in the reaction of $[Ru^{III}(NH_3)_6]/Na_{56}X$ with CO and H_2 (200 and 200 Torr) at 298−393 K: (a) initial spectrum in vacuo, 298 K; (b) 343 K, 20 h; (c) 373 K, 20 h; (d) 393 K, 22 h.

EXAFS Data Characterization of Sample b. To obtain more insight into the structure of the intrazeolitic ruthenium carbonyl dianionic clusters, especially into the metal framework, the EXAFS spectra of the Ru K-edge of sample *b* was analyzed by a curve-fitting method on the basis of the multiple scattering theory.[19] The EXAFS function was obtained from the average X-ray absorption spectra by a cubic spline background subtraction and then normalized through division by the height of the absorption edge. The raw EXAFS data characterizing sample *b* (Figure 5a) show oscillations up to a value of *K*, the wave vector, of about 15 $Å^{-1}$, clearly indicating the presence of near-neighbor high atomic weight backscatterers, which are inferred to be Ru atoms. The Fourier transform (Figure 5b) was obtained from the raw EXAFS data with a K^3-weighting in the range $3.1 < K/Å^{-1} < 15$. The Fourier transformed data were then inversely transformed in the range 1−3.2 Å to R space for isolating the major contributions from low-frequency noise and high-shell contribution. Since the IR data indicated that carbonyl ligands were also present in sample *b*, the peak in the range $1.0 < R/Å < 3.2$ is attributable to a three shell of Ru−Ru, Ru−C, and Ru(−C−)O contributions. Since the Ru(−C−)O contribution was found to be strongly coupled with the Ru−Ru contribution, these two contributions had to be analyzed

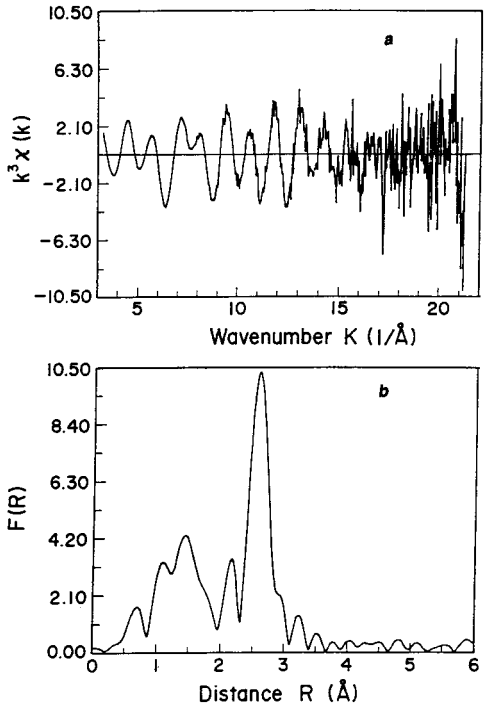

Figure 5. Ru K-edge EXAFS data for synthetic $[Ru_6(CO)_{18}]^{2-}/Na_{56}X$: (a) K^3-weighted EXAFS spectrum $K^3\chi(k)$ vs K; (b) Fourier transform of K^3-weighted EXAFS spectrum $K^3\chi(k)$ vs R, the distance from the absorbing atom.

TABLE 4: Results of the Curve-Fitting Analysis of Ru K-Edge EXAFS Data Obtained at 296 K for $[Ru_6(CO)_{18}]^{2-}/Na_{56}X$

shell	CN	R/Å	$\Delta E°$/eV	σ/Å
Ru−Ru	3.5	2.82	12.85	0.067
Ru−O	3.0	3.01	−5.63	0.052
Ru−C	3.1	1.86	−6.67	0.060
Ru−Oz (zeolite)	0.3	2.26	3.66	0.085

[a] Notation: CN, coordination number for absorber−backscatterer pair; R, radial absorber−backscatterer distance; σ, Debye−Waller factor; $\Delta E°$, inner potential correction (correction of the edge position).

simultaneously. The structural parameters were estimated initially by fitting the data in the high-K range ($8.5 < K/Å^{-1} < 15$). The multiple scattering associated with the Ru(−C−)O group was found to be significant, whereas the Ru−C contribution was insignificant in this range. Further analysis, following subtraction of the calculated Ru−Ru and Ru(−C−)O contributions from the raw data, led to characterization of the Ru−C contribution. The fit of the raw data with the sum of the three contributions was still not satisfactory, and it was inferred that another contribution had to be accounted for. A fourth contribution involved another low atomic number backscatterer, which was assumed to be the oxygen of zeolite, referred to as Ru−Oz. The initial structural parameters characterizing the Ru−C and Ru−Oz contributions were obtained by fitting the residual spectrum. The Ru−Ru, Ru−C, Ru(−C−)O, and Ru−Oz contributions were then determined simultaneously through adjusting of the parameters of the initial estimates. The iteration was continued until good overall agreement was obtained. The results of curve-fitting analyses with the best calculated coordination parameters are shown in Table 4. The data indicate Ru−Ru coordination numbers of 3.5 at an average distance of 2.82 Å, Ru−C coordination numbers of 3.1 at an average distance of 1.86 Å, Ru(−C−)O coordination numbers of 3.0 at an average distance of 3.01 Å, and Ru−Oz coordination numbers of 0.3 at an average distance of 2.26 Å. The average Ru−Ru coordination numbers of 3.5 suggest a cluster containing 4−6 Ru atoms, while the Ru−Ru distance of 2.82 Å is nearly the same as the value found in $[N(PPh_3)]_2[Ru_6(CO)_{18}]$ in the crystalline state (2.80−2.89 Å).[20] Since the coordination numbers for crystalline $[Ru_6(CO)_{18}]^{2-}$ are 4, it can be deduced that about 87% of the Ru atoms of sample *b* are present as an $[Ru_6(CO)_{18}]^{2-}$ cluster, based on the ratio of 3.5:4. The contribution of Ru−Oz indicates that, in addition to $[Ru_6(CO)_{18}]^{2-}$, there are other Ru species formed that are bonded to the framework of the zeolite via oxygen. A reasonable explanation is that the minor species present, along with the dianionic clusters, are mononuclear carbonyl species, which results in an Ru−Ru coordination number of <4.

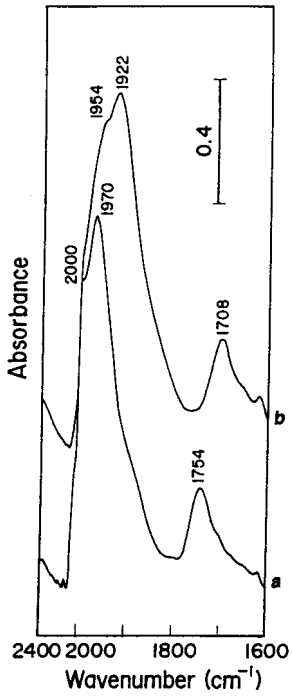

Figure 6. In situ FT-IR spectra obtained for (a) $[Ru_6(CO)_{18}]^{2-}/Na_{56}X$ in vacuo and (b) ^{13}CO isotopic exchange of $[Ru_6(CO)_{18}]^{2-}/Na_{56}X$ during a mixed ^{13}CO and H_2 (20 and 20 Torr) atmosphere at 353 K for 2 h.

On the basis of IR, UV−vis, and EXAFS spectroscopies, we can conclude that the dianionic ruthenium carbonyl clusters were synthesized in $Na_{56}X$ zeolite.

^{13}CO Exchange Reaction and Reversible Regeneration of Sample b. On exposing sample *b* ($[Ru_6(CO)_{18}]^{2-}/Na_{56}X$) to 20 Torr of ^{13}CO and 20 Torr of H_2 at 353 K for 2 h, the bands of terminal CO at 2000 and 1970 cm^{-1} were completely replaced by new bands at 1954 and 1922 cm^{-1}, and the band of bridging CO at 1754 cm^{-1} was replaced by the band at 1708 cm^{-1} (Figure 6, line b). The values of the band shifts after isotopic exchange was 46−48 cm^{-1}, roughly in the range calculated according to the two-atom model ($\Delta\nu$ = 39−44 cm^{-1}). Furthermore, this process was reversible when normal CO and H_2 were introduced under same conditions. These results suggest there is no change in the metal skeleton of sample *b* during isotopic exchange. However, in the absence of hydrogen, isotopic exchange does not proceed.

The structure of $[Ru_6(CO)_{18}]^{2-}$ in the cages is very sensitive to oxygen. When the wafer of sample *b* in the IR cell was brought in contact with 100 Torr of O_2 at room temperature, the bridging CO band at 1754 cm^{-1} quickly disappeared. On raising the temperature to 403 K, the new spectrum was obtained, showing CO bands at 2088 and 2016 cm^{-1} (Figure 7, line b). At the same time, a low-frequency peak at 880 cm^{-1}

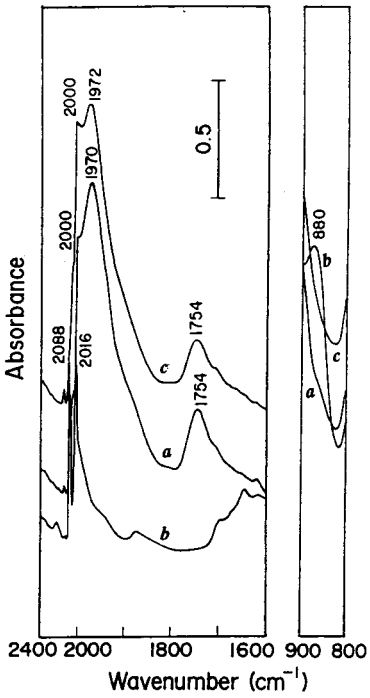

Figure 7. In situ FT-IR spectra characterizing the samples: (a) synthetic $[Ru_6(CO)_{18}]^{2-}/Na_{56}X$; (b) oxidation fragmentation of $[Ru_6(CO)_{18}]^{2-}/Na_{56}X$ during 100 Torr of O_2 at 403 K for 2 h; (c) reductive recarbonylation of oxidized sample during 200 Torr of CO and 200 Torr of H_2 atmosphere at 393 K for 12 h.

is also present, closely resembling 862 cm^{-1} of Figure 3A, line c, which is ascribed to $(CO)_2Ru^I-O-Al(Si)$. However, the 18 cm^{-1} blue shift here is probably associated with the variation of water concentration in $Na_{56}X$ zeolite.[21] $(CO)_2Ru^I-O-Al(Si)$ was recarbonylated in a mixed CO and H_2 atmosphere at 393 K. The IR bands of the resulting sample at 2088, 2000, 1972, and 1754 cm^{-1} (Figure 7, line c) are practically identical to those of $[Ru_6(CO)_{18}]^{2-}/Na_{56}X$ (Figure 7, line a), as seen from comparison of the wavenumbers, intensity, full width at half-maximum (fwhm) of CO bands, and the constant intensity ratio of CO_t:CO_b bands between the initial $[Ru_6(CO)_{18}]^{2-}/Na_{56}X$ and the recarbonylated sample. This indicates that $[Ru_6(CO)_{18}]^{2-}$ was re-formed inside the α-cages. The recarbonylated sample became pale yellow again (λ_{max} = 235 and 287 nm in the UV−vis spectrum). The process was carried out several times without any significant change in the IR spectrum of the carbonylated form. Therefore, we conclude that the oxidative fragmentation and reductive regeneration are reversible under these conditions.

When the organometallic species was extracted from the synthetic sample *a* by hexane and from the sample *b* by CH_2Cl_2 solution, the supernatant solution remained colorless and showed no IR absorption in the CO stretching region. Furthermore, no appreciable CO frequency shifts were observed when $[H_4Ru_4(CO)_{12}]$ or $[Ru_6(CO)_{18}]^{2-}$ was deposited from the organic solution onto the zeolite wafer.

Reaction Kinetics and Product Distribution. Figure 8A shows temperature-programmed hydrogenation (TPH) plots of surface carbonaceous deposits from CH_4 dissociation at 623 K on $[Ru_4]_{red}/Na_{56}Y$ catalyst. The selectivity of C_2 reaches 18.8%, the selectivity of C_3 reaches 1.6%, and the selectivity of C_4 reaches 1.0%. The hydrogenation temperature (*T*) remarkably affected the yield of the C_{2+} hydrocarbons (Figure 8B): for T = 298−373 K, C_{2+} selectivity is more than 30%; for 373 K < T < 473 K, C_{2+} selectivity reaches 17.3%; for 473 K < T < 573 K, C_{2+} selectivity comes up to 22.1%, but non-C_4 species is observed. When T is raised beyond 573 K, the only product is methane. Moreover, it is interesting that the optimum temperature (423 K) for making C_3 is higher than that for making C_4 (373 K) (Figure 8A). This implies that part of C_3 hydrocarbon may be created through hydrogenolysis and/or decomposition of C_4 hydrocarbon.[9]

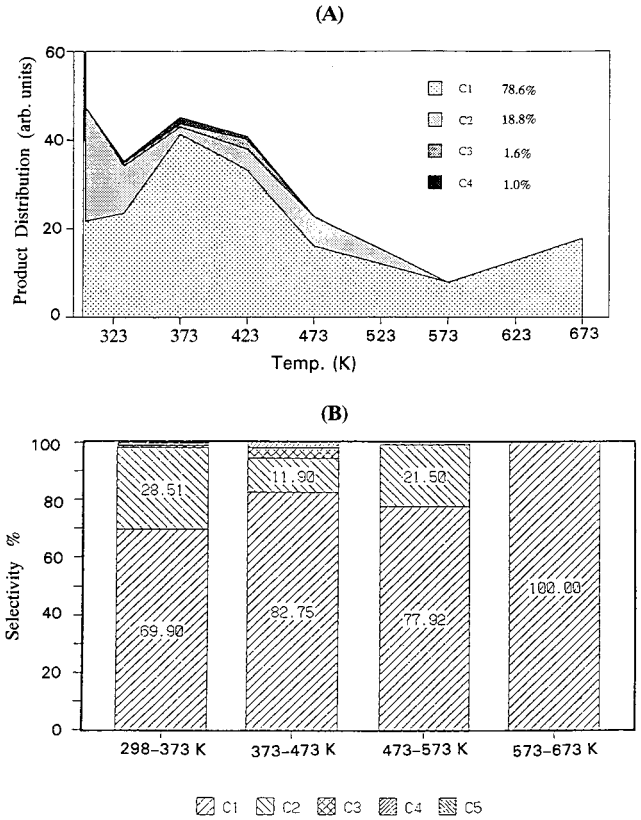

Figure 8. (A) Temperature-programmed hydrogenation (TPH) plots of the surface carbonaceous deposits created from 70 μmol of CH_4 dissociation on $[Ru_4]_{red}/Na_{56}Y$ catalyst at 623 K. (B) Selectivity of alkanes vs range of hydrogenated temperature.

Table 5 lists the kinetic parameters of methane homologation on the intrazeolitie anchoring of Ru clusters. These include methane converting carbonaceous deposits (C_1) and the carbonaceous surface coverage (θ) in the methane dissociation and the carbonaceous deposits conversion (C_2) and C_{2+} selectivity in the hydrogenation of the carbonaceous deposits. To balance the carbons in the reactions, we estimated the real methane conversion by multiplying C_1 and C_2 and the residual carbonaceous deposits by multiplying C_1 and $(1 - C_2)$. For $[Ru_3]_{red}$/NaY, $[Ru_4]_{red}$/NaY, and $[Ru_6]_{red}$/NaY catalysts at CH_4 dissociation temperature of 723 K, C_1 is 27.8%, 25.6%, and 19.2%, respectively; the carbonaceous surface coverage (θ) is 20%, 18%, and 14%, respectively; C_2 reaches 37%, 33%, and 12%, respectively; the C_{2+} selectivity is 14.6%, 13.9%, and 5.3%, respectively; C_1C_2 is 10.3%, 8.4%, and 3.8%, respectively; and $C_1(1 - C_2)$ is 17.5%, 17.2%, and 16.9%, respectively. $[Ru_4]_{red}$/NaY catalyst shows a maximum C_1 of 25.6% at 723 K, a maximum carbonaceous surface coverage of 18% at 723 K, a maximum C_2 of 90% at 523 K, a maximum C_1C_2 of 9.7% at 623 K, and a maximum C_{2+} selectivity of 21.3% at 623 K. Following the parameters of Table 5 at 723 K on $[Ru_6]_{red}/Na_{56}Y$ and $[Ru_6]_{red}/Na_{56}X$ catalysts, $Na_{56}X$ is superior to $Na_{56}Y$ in promoting methane conversion (C_1C_2) and C_{2+} selectivity.

Characterization of Carbonaceous Deposits by TPD, IR, and Mass Spectroscopies. *TPD Spectroscopy.* Methane de-

TABLE 5: Kinetic Parameters of Methane Homologation on the Intrazeolite Anchoring of Ru Clusters Catalysts

samples	CH_4 decomp temp (K)	C_1 (%)	θ [CH_x/Ru]	C_2 (%)[a]	C_{2+} (%)[a]	C_1C_2 (%)	$C_1(1-C_2)$ (%)
$[Ru_3]_{red}/Na_{56}Y$	723	27.8	0.20	37	14.6	10.3	17.5
$[Ru_4]_{red}/Na_{56}Y$	523	7.7	0.05	90	4.8	6.9	0.8
	623	15.6	0.11	62	21.3	9.7	5.9
	723	25.6	0.18	33	13.9	8.4	17.2
$[Ru_6]_{red}/Na_{56}Y$	623	9.3	0.07	47	6.5	4.4	4.9
	723	19.2	0.14	12	5.3	2.3	16.9
$[Ru_6]_{red}/Na_{56}X$	723	22.1	0.16	17	6.1	3.8	18.3

[a] C_{2+} selectivity $= \Sigma nC_n(n=2-4)/\Sigma nC_n(n=1-4)$.

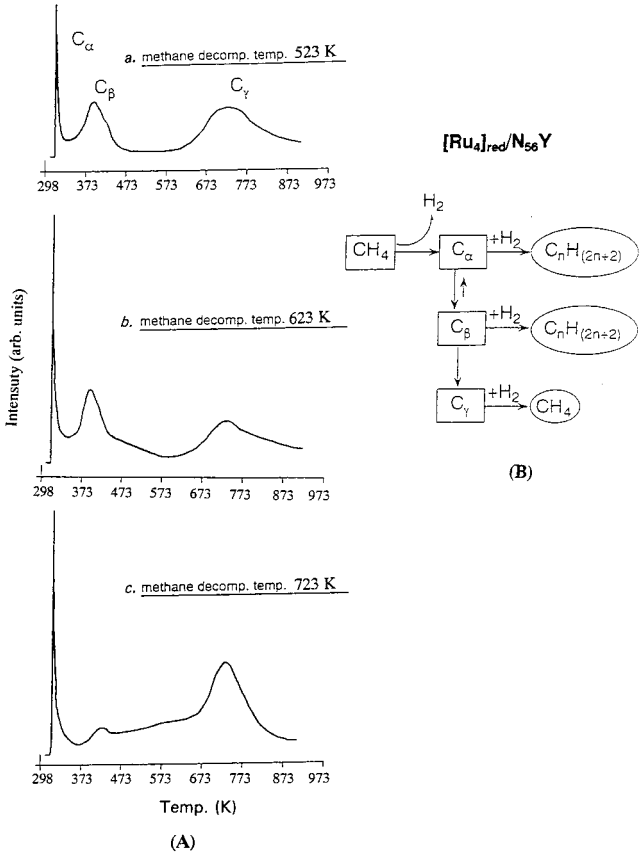

Figure 9. (A) Distinguishability of different kinds of surface carbonaceous deposits from methane dissociation at 523 (a), 623 (b), and 723 K (c) in temperature-programmed hydrogenation (TPH) run. (B) Scheme of inference for activity of the surface carbonaceous species.

composition on transition-metal catalysts can create three different kinds of carbonaceous deposits, as identified by solid-state NMR[22] and atomic emission spectroscopy (AES).[22,23] Here we distinguish three kinds of peaks, denoted as C_α, C_β, and C_γ from the surface deposits by their different hydrogenation temperature on TPH (temperature-programmed hydrogenation) run. The C_α was hydrogenated below 334 K, C_β was hydrogenated from 335 to 573 K, and C_γ reacted above 573 K (Figure 9A). The peak area ratio $(C_\alpha + C_\beta)/C_\gamma$ varies with the dissociation temperature of CH_4, the maximum value of which is reached at 623 K (Figure 9A, part b).

FT-IR Spectroscopy. The IR wafer of $[Ru_4]_{red}$/NaY was exposed to a flow of 20 cm^3/min of diluted CH_4 (5% CH_4 in He) at 523, 623, and 723 K, respectively, and then quickly cooled to 298 K. The in situ FT-IR spectra were recorded. Figure 10b shows the weak bands at 2936, 2890, and 2720 cm^{-1} and middle bands at 1427 and 1332 cm^{-1}. These are due to adspecies from CH_4 dissociation at 523 K. Georeg et al. reported the analogous IR frequency in ethylene and diazomethane thermal chemisorption on Ru(001) surface[24] and acetylene thermal chemisorption on W(110)[23] and Ni(111) surface.[25a] Oxton et al.[25b] showed IR bands of the $-CH_2$ ligand of $(\mu\text{-}CH_2)[C_pCo(CO)_{12}]_2$ clusters at 2981, 2918, 1350, and 1127 cm^{-1} (Table 6). By comparing IR bands of Figure 10b with vibrational bands of modes involving the $-CH_2$ ligands (Table 6), one can reasonably suggest that the 2936 and 2890 cm^{-1} bands are assigned to C−H stretching of CH_2, the 2720 cm^{-1} band is assigned to C−H stretching of CH adspecies, and the 1427 and 1332 cm^{-1} bands are ascribed to the deformation vibration of CH_2 adspecies. Figure 10c,d shows similar bands of $CH_{1,2}$ adspecies as Figure 10b, but with decrease of the band intensities. This implies that the CH_2 and CH fragments diminish with increasing dissociation temperature.

Mass Spectroscopy. To confirm that the carbonaceous deposits were created from CH_4, we have used in situ MS (AQ-200, Anelva Co) spectra to record the deuterium distribution in the deuteration of carbonaceous deposits. Figure 11A clearly shows the distribution of CH_2D_2, CHD_3, and CD_4 in methane, such as CH_2D_2 (18%), CHD_3 (7%), and CD_4 (75%) are obtained at 323 K. The deuterated activity of the carbonaceous deposits varies with the deuteration temperature. These suggest that carbonaceous deposits include CH_2, CH, and carbon fragments (Figure 11B).

Discussion

Confirmation of Ruthenium Carbonyl Clusters in Zeolite Cages. The synthetic zeolitic $[H_4Ru_4(CO)_{12}]$ showed the terminal CO stretching bands at 2085 (axial), 2070, 2031, 2008, and 1992 cm^{-1} (equatorial). The 17 cm^{-1} red shift (2009 → 1992 cm^{-1}) of the equatorial CO band, the 5 cm^{-1} blue shift (2080 → 2085 cm^{-1}) of the axial CO band, and CO bands broadening and intensity variation were observed referencing those of $[H_4Ru_4(CO)_{12}]$ in hexane solution (Figure 1A and Table 1). The characteristic variation of the equatorial CO band shown in $[H_4Ru_4(CO)_{12}]/Na_{56}Y$ is similar to that of metal carbonyls in solution containing Lewis acids, such as $Al(C_2H_5)_3$, which have been examined extensively.[26] The equatorial terminal CO ligands are more basic than axial terminal CO ligands,[27] which may causes a reaction mainly with extraframework Na^+ cations and with possible Lewis acid (Al^{3+} ions) formed by dehydration of $Na_{56}Y$,[5,7,8] through involvement of the oxygen end of the equatorial CO ligands. Such an interaction is expected to result in a net electron withdrawal from the clusters, a decrease in back-bonding to the axial terminal CO ligands, a strengthening of the carbon−oxygen bond, and a shift of axial terminal CO bands to higher frequencies.

The IR bands of $[Ru_6(CO)_{18}]^{2-}$ were observed either in solution (2006 (s), 1986 (vs), 1930 (m), and 1754 cm^{-1} (w)) or in $Na_{56}X$ cages (2000 (s), 1972 (vs), 1925 (m), and 1747 cm^{-1} (w)), as summarized in Table 3. However, the stretching frequency (1747 cm^{-1}) of the bridging CO ligands in $[Ru_6(CO)_{18}]^{2-}/Na_{56}X$ are shifted to lower energy by approximately 7 cm^{-1} compared to that of $[Ru_6(CO)_{18}]^{2-}$ (1754 cm^{-1}) in CH_2-

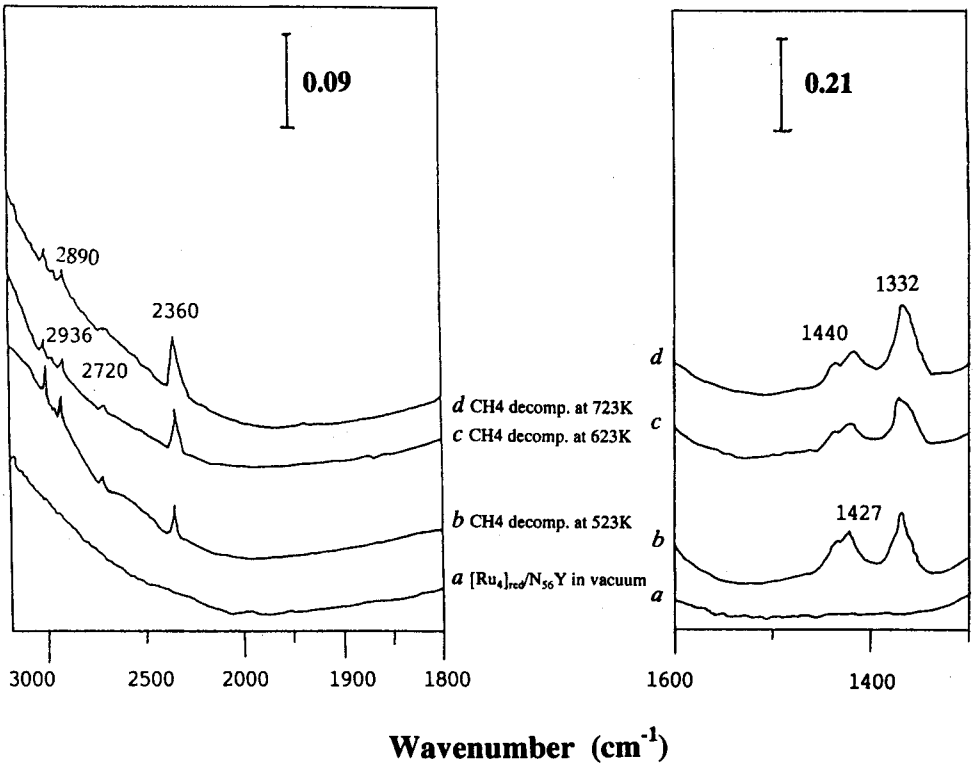

Figure 10. In situ FT-IR spectra of CH_4 dissociation at 523 (b), 623 (c), and 723 K (d) on $[Ru_4]_{red}/Na_{56}Y$ catalyst.

TABLE 6: Mode Assignments for CH_4 Thermal Dissociation on $[Ru_4]_{red}/Na_{56}Y$ Compared to Those of Ethylene, Diazomethane on Ru(001), and Relevant Organometallic Complexes (in wavenumbers/cm^{-1})

mode	CH_2 on Ru(001)[a]	CH_2 Co – Co	CH_2 Os – Os	CH_2 Ru – Ru
CH_2 wag	1135	1127	961	1332
CH_2	1450	1350	1428	1427
$\nu_s(CH_2)$	2940	2918	2935	2890
$\nu_a(CH_2)$	3050	2981	2984	2936
ref	23	23	24b	this work

[a] CH_2 from both C_2H_4 and CH_2N_2.

Cl_2 solution. This shift could be consistent with the formation of ion pairs with extraframework Na^+ cations or with Lewis-acid sites (Al^{3+} ions). In contrast to previous results,[5–8] the terminal CO bands unexpectedly shifted to lower frequency. A tentative explanation is that under the synthesis conditions almost all the water is removed, as evidenced by the IR spectrum (Figure 3A, line d). Presumably, most of the $Na_{56}X$ cage cations are not hydrated and behave as Lewis acids, interacting with not only the more strongly basic bridging CO ligands but also the less basic terminal CO ligands of the ruthenium cluster dianion.

One of the main issues complicating the synthesis and characterization of metal clusters in zeolites is the possible simultaneous formation of metal clusters or crystallites on the exterior of zeolite. However, the results of the work here suggest that virtually all the ruthenium carbonyl clusters were formed and confined to the zeolite cages. Extraction of the organometallic species from synthetic samples by hexane or CH_2Cl_2 solution was unsuccessful. The results are consistent with a "ship-in-a-bottle" synthesis of the ruthenium carbonyl clusters: the precursor $[Ru^{III}(NH_3)_6]$ or $[Ru_3(CO)_{12}]$ is presumed only to be located inside the α-cages by its molecular size under ion exchange or vapor dispersion preparation. The synthetic

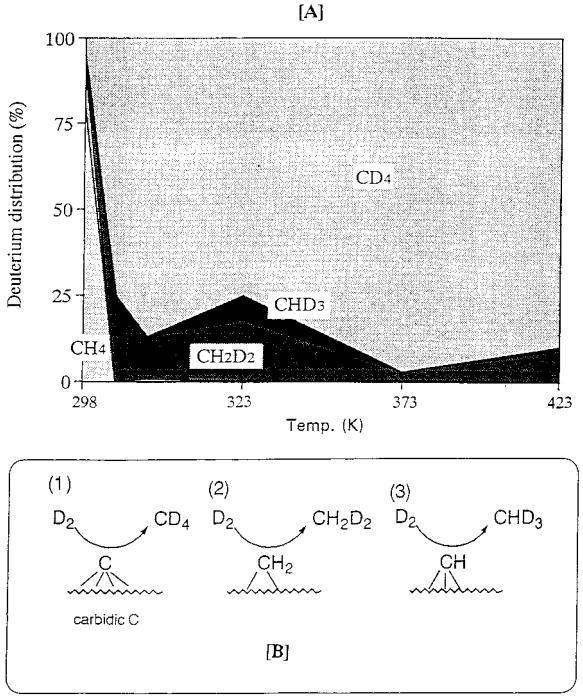

Figure 11. (A) Deuterium distribution of methane vs temperature in temperature- programmed deuteration run. (B) Model of the surface carbonaceous species deuteration on $[Ru_4]_{red}/Na_{56}Y$ catalyst.

$[H_4Ru_4(CO)_{12}]$ or $[Ru_6(CO)_{18}]^{2-}$ cluster is small enough to fit in the α-cages of $Na_{56}X$ but too large to match the β-cage and hexagonal prisms and to diffuse through the apertures. No IR band shifts were observed between crystalline Ru carbonyl clusters and their site of deposition onto the extrazeolite. Therefore, present IR band shifts imply that the $[H_4Ru_4(CO)_{12}]$ or $[Ru_6(CO)_{18}]^{2-}$ should be encapsulated in the α-cages. Assuming the synthetic $[Ru_6(CO)_{18}]^{2-}$ located on the extrazeolite, the reversible re-formation of $[Ru_6(CO)_{18}]^{2-}$ resulting from

CO and H_2 chemisorption on its oxidation state will be unsuccessful, since extrazeolitic Ru clusters cause coalescence under our reductive regeneration conditions.

Mechanism of Ruthenium Carbonyl Clusters Formation in Zeolite Cages. *Formation of [Ru4H4(CO)12]/Na56Y.* Treatment of $[Ru_3(CO)_{12}]$ with H_2 gave $[Ru_4H_4(CO)_{12}]$ conveniently in high yield and purity. Excellent analytical data were obtained for sample *a*, which displayed five CO bands in the IR spectrum (Figure 1A, line b, and Table 1). The CO/Ru stoichiometry of about 3 mol of evolved CO to 1 mol of $[Ru_3(CO)_{12}]$ (where the stoichiometry is derived from detection by gas chromatography) is consistent with the surface reaction

$$4Ru_3(CO)_{12} + 6H_2 \xrightarrow{363\ K,\ 24\ h} 3Ru_4H_4(CO)_{12} + 12CO \quad \text{(i)}$$

$$CO/Ru_3 \text{ molar ratio} = 3$$

involving the nucleation of the starting Ru_3 cluster into the Ru_4 hydrido species.

As expected, $Na_{56}Y$ encapsulated $[Ru_3(CO)_{12}]$ demonstrated fair activity, being converted to $[Ru_4H_4(CO)_{12}]$ in hydrogen atmophere at 363 K. Higher reaction temperature should, however, be avoided, since $[Ru_4H_4(CO)_{12}]$ starts to decompose to metallic Ru above 383 K. Knox et al.[28] showed that $[Os_3(CO)_{12}]$ in octane solution at 393 K, under hydrogenation, formed $[Os_3H_2(CO)_{10}]$ as the first step. $[Os_4H_4(CO)_{12}]$ was subsequently obtained by additional treatment of the trinuclear hydride cluster with H_2. A remarkable peculiarity of the $Na_{56}Y$ internal surface-mediated route is that $[Ru_3H_2(CO)_{10}]$ does not seem to be formed as a stable intermediate in the α-cages, as determined by our IR spectrum. The unstable $[Ru_3H_2(CO)_{10}]$ quickly reacted with H_2 at 363 K to form $[Ru_4H_4(CO)_{12}]$.

In addition, a mechanism of $[H_4Ru_4(CO)_{12}]$ formation involving surface-OH groups of the α-cages cannot be ruled out. However this reactivity, leading to the formation of the grafted surface species $HM_3(CO)_{10}(OSi\leqslant)$, is possible only in the absence of hydrogen, according to the oxidative addition of a silanol group into a metal−metal bond of the cluster frame.[29] The surface-OH group chemisorbed cluster does not transform into $[H_4M_4(CO)_{12}]$ if subsequently heated in a hydrogen atmosphere. Consequently, in the reported synthesis of $[H_4M_4(CO)_{12}]$ inside the α-cages, it is very important to avoid any chemical interaction of the cluster precursor with the −OH group of the framework. As a result of $[H_4Ru_4(CO)_{12}]$ observations, we believe that the internal topology of zeolite is likely to play a significant role in the stabilization and consequently in the selective formation of organometallic compounds.

Ru(NH3)6Cl3 Reductive Carbonylation in Zeolite Cages. Hexammineruthenium(III) in $Na_{56}X$ zeolite was very unstable under CO and H_2 atmospheres. As shown in Figure 3A, line b, on raising the temperature to 353 K, a major carbonyl stretching vibration at 1939 cm^{-1} appears, which can be assigned to $[Ru^{II}(NH_3)_5(CO)]$ in $Na_{56}X$ zeolite.[14b,18] The band at 1468 cm^{-1} indicated that some of the NH_3 ligands were released from the coordination sphere of the complex, forming NH_4^+ ions,[14b] while the intensity of the 1640 and 1356 cm^{-1} bands due to NH_3 ligands decreased.[14b] The diffuse reflectance spectrum at 390 and 280 nm also showed the presence of an $[Ru^{II}(NH_3)_5(CO)]$ intermediate (Figure 4, line b). When the temperature reached 393 K for 30 min, the CO band (1393 cm^{-1}) of $[Ru^{II}(NH_3)_5(CO)]$ disappeared, and two double carbonyl bands emerged at 2088, 2014 and 2048, 1952 cm^{-1}, which are attributed to bicarbonylruthenium(I) and tricarbonylruthenium(I) in $Na_{56}X$ zeolite, respectively.[14b,18] It is noteworthy that the IR spectrum of ruthenium carbonyl intermediate showed a low frequency at 862 cm^{-1}, which is ascribed to the adduct of mononuclear ruthenium carbonyl species with the oxygen of $Na_{56}X$ framework, either $(CO)_2Ru^I-O-Al(Si)$ or $(CO)_3Ru^I-O-Al(Si)$ (see following discussion for details). Bicarbonylruthenium(I) and tricarbonylruthenium(I) were converted into dianionic ruthenium carbonyl clusters after 22 h at 393 K, while the lower frequency 862 cm^{-1} disappeared. The reflectance UV−vis spectrum is in good agreement with IR results, giving two absorption bands at 235 and 287 nm (Figure 4, line d), being practically identical to those of $[PPN]_2[Ru_6(CO)_{18}]^{2-}$ in THF (235 and 285 nm in Table 2). EXAFS analysis also confirmed the final formation of $[Ru_6(CO)_{18}]^{2-}$ in $Na_{56}X$ zeolite. On the basis of these analyses, we propose that the mechanism of $Ru^{III}(NH_3)_6$ reductive carbonylation is as shown in eqs ii and iii.

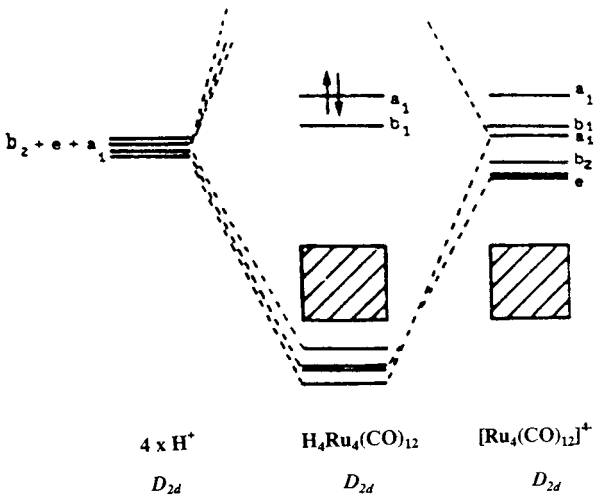

Figure 12. Schematic representations of the molecular orbitals for hydrido metal carbonyl clusters derived from extended Huckel molecular orbital calculations.

$$[Ru^{III}(NH_3)_6]/Na_{56}X \xrightarrow{ii} [Ru^{II}(NH_3)_5(CO) + Ru^I(CO)_2 + Ru^I(CO)_3]/Na_{56}X \xrightarrow{iii} [Ru_6(CO)_{18}]^{2-}/Na_{56}X$$

Electronic Structure and Spectra of Ruthenium Carbonyl Clusters. *[Ru4H4(CO)12]/Na56Y.* $[Ru_4H_4(CO)_{12}]$ is a D_{2d} geometry with edge-bridging hydrides established through X-ray diffraction.[30] Hoffmann et al.[31] calculated the energy of the frontier orbitals of $[Ru_4(CO)_{12}]^{4-}$ using the extended Huckel method, as shown in Figure 12. In each geometry the $a_1 + b_1 + a_1 + b_2 + e$ (where $b_1 + a_1$ result from the e level of T_d $[M_4(CO)_{12}]^{4-}$ and $b_2 + e$ result from the t_2 level of T_d $[M_4(CO)_{12}]^{4-}$) occupied set of cluster orbitals is at high energy, fairly well separated from other orbitals. This supports the general picture of bonding in such a cluster that has been observed previously.[32,33] In $[Ru_4H_4(CO)_{12}]$, four protons coming in along the edge, each bearing a 1s orbital, transform as $a_1 + b_2 + e$. The overlap of an incoming proton with the framework orbitals of the tetrahedron gives the MO scheme in Figure 12.

The absorption band for $[Ru_4H_4(CO)_{12}]$ inside the α-cages gave a maximum peak at 364 nm (Figure 2), which is close to the $\sigma^{*\prime} \rightarrow \sigma^*$ transition observed for $[Ru_4H_4(CO)_{12}]$ in solution (360 nm, Table 2). However, there is a 4 nm red shift of the $\sigma^{*\prime} \rightarrow \sigma^*$ transition. This may be considered to be the Na^+ and/or Al^{3+} ions effect on the band energy involving states best described as M−M ($\sigma^{*\prime} \rightarrow \sigma^*$) and M−CO.[19] The effect of

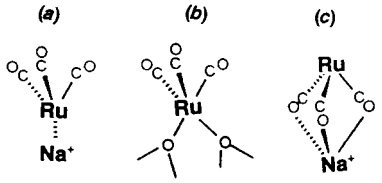

Figure 13. Three models concerned with possible anchoring sites of the α-cage located intermediate, $Ru^I(CO)_3/Na_{56}X$.

Na^+ and/or Al^{3+} cations binding to the oxygen end of the carbonyl ligand is expected to weaken the CO π-bond stretching energy (red shift of IR CO bands in Figure 1A, line b) and to withdraw net electrons from the Ru cluster, which is expected to make it less antibonding. Consequently, the transition energy of M−M bonds should decrease on passing to $[H_4Ru_4(CO)_{12}]/Na_{56}Y$.

Intermediate $Ru^I(CO)_3/Na_{56}X$ and $[Ru_6(CO)_{18}]^{2-}/Na_{56}X$. A detailed derivation of the molecular orbitals for an ML_3 fragment has been given elsewhere.[34] We briefly note the salient features of the analysis. The $M(CO)_3$ fragment is considered in C_{3v} regular trigonal-pyramidal geometry, with C−M−C angles of 90°. The coordinate system is a set of three low-lying orbitals, $a_1 + e$, comprising mainly of z^2 ($1a_1$), *xy*, and $x^2 - y^2$ ($1e_1$).[34] The π^* orbitals on the carbonyls interact in phase with these three. At somewhat higher energy there is an e set of largely *xz* and *yz* character (2e) which are antibonding to the σ levels of the ligands. Finally, at still higher energy is an sp hybrid orbital ($2a_1$).

Three models can be considered for possible anchoring sites of the α-cage located $Ru^I(CO)_3$, as illustrated in Figure 13. Two of these candidates, *a* and *c*, involve interaction of the $Ru^I(CO)_3$ fragment with an extraframework Na^+ cation, the former with direct binding of the metal center of the tricarbonyl moiety to the Na^+ cation and the latter with indirect binding through the oxygen end of the carbonyls to the Na^+ cation. The third model *b* bypasses the extraframework cations altogether and considers the immobilization of the tricarbonylmetal moiety on the oxygen of zeolite, over a vacant six- or four-ring site devoid of an adjacent extraframework cation. Ozin et al.[15] argued against structures *a* and *c* and by a process of deductive elimination strongly favored structure *b* using far-IR determination of CO bond stretching with varying cation ionic potential down the series Li^+ to Cs^+. The $Ru^I(CO)_3$ moiety attached to the framework via lattice oxygens is also considered to be consistent with the charge balance. Our EXAFS data (Table 4) indicated that sample *b* has a Ru−Oz coordination number of 0.3 with an average Ru−Oz distance of 2.26 Å. Since the framework oxygens are proposed to anchor mononuclear ruthenium carbonyl species, there is Ru−Oz coordination numbers of 2.0 for 13% mononuclear ruthenium carbonyl species. These provide an informative picture of the intrazeolitic anchoring of $Ru^I(CO)_3$ intermediate, which includes the effect of bringing two oxygen ligands in a C_{3v} arrangement up to the C_{3v} $Ru^I(CO)_3$ fragment to form the postulated C_{3v} five-coordinate representation of anchoring site *b* in Figure 13. As a framework oxygen atom contains both $2p\sigma$ and $2p\sigma$ donor orbitals lying at lower energy than the filled valence $a_1 + e$ set of the $Ru^I(CO)_3$ fragment, one can visualize that the major effect of the attachment of $Ru^I(CO)_3$ to a zeolitic oxygen framework site will cause the energy of the empty valence $2a_1 + 2e$ σ set of orbitals to rise with a parallel but lesser effect on the filled valence $1a_1 + 1e$ π set.[15] Consequently, the original HOMO−LUMO energy gap of the naked $Ru^I(CO)_3$ fragment, denoted Δ, must increase on passing to $Ru^I(CO)_3-Na_{56}X$.[35,36] These patterns are borne out in the transformation of C_{3v} to C_s geometries for $M^I(CO)_3/Na_{56}X$.[15] The λ_{max} of the unique feature ($\lambda_{max} = 240$ and 340 nm; Figure 4, line c) would correspond to the framework oxygen anchoring of $Ru^I(CO)_3$ in its C_s form. Further, the ν_{CO} middle IR spectrum of $Ru(CO)_3L_2$ complexes (where L = O, N is a donor ligand) are very similar to those of $Ru^I(CO)_3/Na_{56}X$, which also supports our proposed structure *b* in Figure 13.

Because of the difficulty of precise molecular orbital calculation and satisfactory assignment of specific electronic transitions in this extensive $[M_6(CO)_{18}]^{2-}$ series, it did not prove feasible to extract useful information on the metal−metal and metal−CO energies. Despite this, Green et al.[33] have provided some evidence, in which the first ionization energy of $[Ru_6(CO)_{18}]^{2-}$ is only 0.3 eV lower than that of $[Ru_3(CO)_{12}]$. This suggests that the molecular frontier orbitals of $[Ru_6(CO)_{18}]^{2-}$ may closely resemble those of $[Ru_3(CO)_{12}]$. The band was observed near 290 nm in the spectrum of $[Ru_6(CO)_{18}]^{2-}/Na_{56}X$ (Figure 4, line d, and Table 2). This is characteristic of electronic transitions associated with the metal−metal bonds in this sample. Interaction involving Na^+ and/or Al^{3+} cation binding to the oxygen end of the bridging carbonyl ligand is expected to cause a decrease in M−CO π^*-back-bonding and in the transition energy of the cluster Ru−Ru bond, referencing free $[Ru_6(CO)_{18}]^{2-}$. However, unlike $[Ru_3(CO)_{12}]/Na_{56}Y$,[36] the reflectance spectra do not show any significant red shift, which may be consistent with the assignment of the hexaruthenium aggregation effect of $[Ru_6(CO)_{18}]^{2-}/Na_{56}X$.

Methane Homologation on the Intrazeolite Anchoring of Ru Clusters. Oxidation coupling of methane to ethylene has been proposed as a promising alternative route[37,38] and proceeds at temperatures above 850 K. In addition, this chemical route creates a reaction environment conductive to deep oxidation of CH_4 and higher hydrocarbons to CO and CO_2. Of interest are recent experiments demonstrating that hydrocarbon formation is possible at low temperature once methane is activated at high temperature.[39−41] We explored the formation of alkanes from methane at atmospheric conditions in a two-step route. At a temperature between 523 and 723 K, methane is decomposed on the intrazeolitic Ru clusters into hydrogen and the carbonaceous deposits (Figures 9 and 10). Subsequently, a particular surface carbonaceous deposits generates hydrocarbons upon hydrogenation at 298−673 K.

In TPD spectroscopy, the surface carbonaceous (C_α) was hydrogenated below 334 K and formed C_{2+} hydrocarbons. A less reactive amorphous carbonaceous layer (C_β) was hydrogenated from 335 to 573 K and produces only traces of C_{2+} hydrocarbons. Unreactive graphitic carbon (C_γ) reacted above 573 K to produce only methane (Figure 9A, part b, and Figure 9B). IR and mass spectroscopies confirmed that CH_2, CH, and C adspecies are a characteristic of CH_4 thermal dissociation. Mass spectroscopy showed a higher selectivity of CH_2 species at lower temperature and a higher selectivity of C species in higher temperature (Figure 11). On the basis of a comparison of mass and TPD spectroscopies, we suggest that reactive C_α ascribes to CH_2 and CH species and less reactive C_β ascribes to active carbon species, whereas C_γ is unreactive carbon.

A moderate dissociation temperature of CH_4 resulted in high selectivity of CH_2 or C_α species, which generated higher methane conversion (C_1C_2) and C_{2+} hydrocarbons, whereas the high-temperature resulted in a greater C_γ species, which hydrogenated with greater difficulty into C_{2+} hydrocarbons (Table 5 and Figures 8−11). These suggest CH_2 adspecies having a relatively low reactivity of ruthenium−carbon,[42,43] being more mobile[44] and more combinative to adjective CH_x

groups at low temperature. In addition, the hydrogenation temperature is also an important parameter in determining the methane conversion (C_1C_2) and C_{2+} selectivity. For example, by raising the temperature from 298 to 335 K, C_{2+} selectivity reached a maximum value (Figure 8B). The methane conversion (C_1C_2) and C_{2+} selectivity are therefore controlled by the C_α carbonaceous and the hydrogenation temperature (Table 5).

In comparison with our previous methane homologation on the intrazeolite anchoring of Co clusters,[9] three features should be noticed: (1) CH_2 and CH species of the carbonaceous deposits on the Ru clusters, is less than that on the Co clusters; (2) in correspondence with (1), the methane conversion (C_1C_2) and C_{2+} selectivity on the Ru clusters are less than those on the Co clusters; and (3) the heavy alkanes are favored on the Co clusters rather than on the Ru clusters.

It is not known whether the catalytic properties of metallic particles are size-dependent as the particles become too small (diameters <10 Å), which is considered quasi-molecular rather than metallic. Here, we investigated the catalytic behavior of precisely defined clusters of just three, four, and six Ru atoms inside zeolite cages, determining their different catalytic activity. $[Ru_6]_{red}/Na_{56}Y$ cluster was 4 times less active (C_1C_2) than $[Ru_4]/Na_{56}Y$ or $[Ru_3]/Na_{56}Y$ clusters. $[Ru_3]_{red}/NaY$ showed maximum methane conversion (C_1C_2) and C_{2+} selectivity (Table 5). This suggests that the catalytic properties of the intrazeolitic Ru clusters is size-dependent for methane homologation as is consistent with the observations of the unique reactivity of size-selected gas-phase metallic clusters.

The combination of the catalysis of Ru clusters with the steric constraints imposed by the zeolite structure carried great potential for activity and selectivity in the methane homologation. The cages allowed the CH_x ($x = 0$, 1, or 2) species to migrate on the surface of Ru clusters without diffusion, due to the constraint of the zeolite channels. This resulted in CH_x species hydrogenating to the desired C_{2+} hydrocarbons. The evidence of support effects is consistent with $Na_{56}X$ being superior to $Na_{56}Y$ zeolite (Table 5). This may be ascribed to the fact that the $Na_{56}X$ host is sufficiently basic to provide an efficient medium and potential in methane homologation. This is consistent with the inference that the interaction of the metallic clusters with a basic support results in an increase in the electron density of the metallic clusters, which favors the catalysis of methane homologation.[45]

Experimental Section

Sample Preparation. *Sample a.* A partial pressure of H_2 (400 Torr) was introduced into the $[Ru_3(CO)_{12}]/Na_{56}Y$ sample (where $Na_{56}Y$ = HSZ-320NAA, lot no. D1-9915, Si/Al = 3.0, surface area 910 $m^2\ g^{-1}$),[36] which did not produce any significant effect or color change at room temperature even after 100 h. However, when the temperature was raised to 363 K, a relevant vaporization immediately occurred. After 24 h under a H_2 atmosphere, the IR and diffuse reflectance spectrum identified different bands of the yellow sample which is denoted sample *a* (3.2 wt % Ru loading).

Sample b. $Ru(NH_3)_6^{3+}$-exchanged $Na_{56}X$ $[Ru(NH_3)_6^{3+}/Na_{56}X$, 3.2 wt % Ru] was prepared by slow addition of an aqueous solution of $Ru(NH_3)_6Cl_3$ (Strem Chemical Co.) to an $Na_{56}X$ slurry (Union Shown K. K. 13X, lot no. 9380113, Si/Al = 1.6, surface area 870 m^2g^{-1}) with rapid stirring of 3 h. The ion exchange was continuously performed for another 48 h at room temperature. This was then filtered, washed free of Cl^{-1} ions with deionized H_2O, and dried in air at room temperature.

The $Ru(NH_3)_6^{3+}/Na_{56}X$ was exposed to 200 Torr of CO and 200 Torr of H_2 in a closed circulation system and heated from 300 to 393 K. After 22 h, the carbonylated sample changed from red to pale yellow and showed stable IR carbonyl stretching frequencies. This is denoted sample *b*.

The concentration of Ru in samples *a* and *b* was determined using an inductively coupled plasma atomic emission (ICP) spectrometer. Attempts to extract organometallic species from sample *a* was carried out by hexane solution and from sample *b* by dichloromethane (CH_2Cl_2) solution.

Characterization of Samples. *IR Spectroscopy.* In situ IR spectra of the samples were recorded with a Shimadzu FT-IR 4200 double-beam spectrometer with 20−100 co-added scans at 2 cm^{-1} resolution. The sample was pressed into a self-supporting wafer (8 mg cm^{-2}) in an N_2 atmosphere box and mounted in a quartz IR cell with CaF_2 windows that was connected to a vacuum-closed circulating Pyrex glass line (10^{-5} Torr). The IR cell was equipped with an electric heater and a liquid N_2 reservoir for high- and low-temperature measurements. The contribution of the gas phase was compensated by using a reference IR cell having the same optical length as the sample cell. ^{13}CO isotopic exchange reactions were performed in the IR cell using enriched ^{13}CO (98%) purchased from Merck Reagent Co. Ltd. Before use, all gases were passed through traps to remove water and/or oxygen.

EXAFS Spectroscopy. EXAFS measurements were carried out at the Photon Factory in Japan National Laboratory for High Energy Physics (KEF-PF) using synchrotron radiation with an electron energy of 2.5 GeV at currents of 80−150 mA. The amount of sample in a wafer was calculated at the Ru−K absorption edge, and the sample wafers were stored in specially designed Pyrex glass cells with Kapton film windows (50 nm thick). The spectra at the Ru−K edge were measured at 296 K under vacuum using an Si(111) double-crystal monochromator. The reference samples used were crystalline $[PPN]_2[Ru_6(CO)_{18}]$ and Ru foil.

EXAFS Data Analysis. The EXAFS data were extracted from the measured absorption spectra by standard methods.[46,47] The normalization was done by dividing the absorption intensities by the height of the absorption edge and subtracting the background using cubic spline routines. The final EXAFS function was obtained by averaging the individual background-subtracted and normalized EXAFS data (two scans for each sample). The main contributions to the spectra were isolated by inverse Fourier transformation of the final EXAFS function over a selected range in *R* space. The analysis was performed on these Fourier-filtered data using empirical parameters (the phase shift and backscattering amplitude functions) obtained from reference samples. The parameters characterizing high-*Z* (Ru) and low-*Z* (C, O) contributions were reliably determined by multiple-shell fitting in *k* space (*k* is the wave vector) and *R* space (*R* is the distance from the absorbing atom) with application of K^3 weighting of the Fourier transform. The accuracy of the parameters were estimated as $0.02 < \sigma < 0.08$ and $-10 < \Delta E° < 10$. The residual factor $\int|k^3\chi^{obs}(k) - k^3\chi^{calc}(k)|^2\ dk/\int|k^3\chi^{obs}(k)|^2\ dk$ was less than 15% for optimized coordination numbers and bond lengths.[47]

Diffuse reflectance spectra were recorded on a Shimadzu UV-2200 series spectrometer with a photomultiplier detector. $BaSO_4$ was used as a reference. The samples were stored in U-type Pyrex glass cells with Heraeus Amersil quartz windows for measurement of evacuation and adsorption.

Methane Homologation. *The Reaction Procedure.* A hundred milligrams of sample *a*, sample *b*, or $[Ru_3(CO)_{12}]/Na_{56}Y$ was placed in the reactor and decarbonylated in a stream of 5% H_2 and 95% He, heated at 5 K/min to 623 K, and then kept

at 623 K for 2 h. The reduced samples obtained are denoted as $[Ru_4]_{red}/Na_{56}Y$, $[Ru_6]_{red}/Na_{56}X$, and $[Ru_3]_{red}/Na56Y$, respectively (where subscripts 4, 6, and 3 only signify the reduced samples resulting from $[Ru_6(CO)_{18}]^{2-}/Na_{56}X$, $[H_4Ru_4(CO)_{12}]/Na_{56}Y$, and $[Ru_3(CO)_{12}]/Na_{56}Y$).

After reduction, the sample with adsorbed H_2 was flushed with He at 300 K for 30 min. The temperature of the reaction was raised under flowing He. The procedure was then switched to a pulsed gas containing dilute CH_4 by He. After methane dissociation, the catalyst was quickly cooled to room temperature under He flow to avoid aging of the surface carbonaceous deposits. The surface carbonaceous deposits were subsequently hydrogenated in a H_2 flow of 20 cm^3 (STP)/min from 298 to 673 K. Before entering the catalyst bed, the gases (He, CH_4, and H_2) were purified through manganese oxide and molecular sieve. The effluent gases from the reactor were stored in loops and were determined afterward by Shimadzu GC-8A gas chromatography with a flame ionization detector.

Characterization of the Surface Carbonaceous Deposits. After the methane decomposition on $[Ru_4]_{red}/Na_{56}Y$ at 523, 623, or 723 K, the surface carbonaceous deposits were hydrogenated on TPH (temperature-programmed hydrogenation) run. The effluent gases were directly determined by a flame ionization detector of Shimadzu GC-8A gas chromatography (where no column separation of the effluent gases occurred). The surface carbonaceous deposits were deuterated with a temperature-programmed heating from 298 to 423 K. The collected gases were analyzed by in situ mass (AQ-200, Anelva Co.) spectroscopy.

References and Notes

(1) Anderson, J. R. *Structure of Metallic*; Academic Press: New York, 1975.

(2) Boudart, M.; Djega-Mariadassou, G. *Kinetics of Heterogeneous Catalytic Reactions*; Princeton University Press: Princeton, NJ, 1984.

(3) Shen, G. C.; Fujita, S. I.; Takezawa, N. *J. Catal*. **1992**, *138*, 754.

(4) Shen, G. C.; Fujita, S. I.; Matsumoto, S.; Takezawa, N. *J. Mol. Catal*. **1997**, *124*, 123.

(5) Shen, G. C.; Shido, T.; Ichikawa, M. *J. Phys. Chem*. **1996**, *100*, 16947.

(6) Shen, G. C.; Liu, A.-M.; Shido, T.; Ichikawa, M. *Top. Catal.* **1995**, *2*, 141.

(7) Rao, L.-F.; Fukuoka, A.; Kosugi, N.; Kuroda, H.; Ichikawa, M. *J. Phys. Chem.* **1990**, *94*, 5317.

(8) Beutel, T.; Kawi, S.; Purnell, K.; Knözinger, H.; Gates, B. C. *J. Phys. Chem.* **1993**, *97*, 7284.

(9) Shen, G. C.; Ichikawa, M. *J. Chem. Soc., Faraday Trans*. **1997**, *93*, 1185.

(10) Ozin, G. A. In Materials Chemistry; Interrante, L. V., Casper, L. A., Ellis, A. B., Eds.; American Chemical Society: Washington, DC, 1995; pp 335−371.

(11) (a) Dossi, C.; Psaro, R.; Roberto, D.; Ugo, R.; Zanderighi, G. *Inorg. Chem.* **1990**, *29*, 4368. (b) Knox, S. A. R.; Koepke, J. W.; Andrews, M. A.; Kaesz, H. D. *J. Am. Chem. Soc*. **1975**, *97*, 3942.

(12) Geoffroy, G. L.; Gladfelter, W. L. *J. Am. Chem. Soc*. **1977**, *99*, 7565.

(13) Nakamoto, K. *Infrared and Raman Spectra of Inorganic and Coordination Compounds*, 3rd ed.; Wiley: New York, 1978; p 199.

(14) (a) Shen, G. C.; Ichikawa, M. *J. Phys. Chem.* **1996**, *100*, 14265. (b) Verdonck, J. J.; Schoonheydt, R. A.; Jacobs, P. A. *J. Phys. Chem*. **1983**, *87*, 683.

(15) Ozkar, S.; Ozin, G. A.; Moller, K.; Bein, T. *J. Am. Chem. Soc*. **1990**, *112*, 9575.

(16) (a) Kurodo, Y.; Kotani, A.; Maeda, H.; Moriwaki, H.; Morimoto, T.; Nagao, M. *J. Chem. Soc., Faraday Trans*. **1992**, 1583. (b) Li, C.; Domen, K.; Maruya, K.; Onishi, T. *J. Am. Chem. Soc*. **1989**, *111*, 7683.

(17) (a) Eady, C. R.; Johnson, B. F. G.; Lewis, J.; Malatesta, M. C. *J. Chem. Soc., Chem. Comm*. **1976**, 945. (b) Eady, C. R.; Jackson, P. F.; Johnson, B. F. G.; Lews, J.; Malatesta, M. C. *J. Chem. Soc., Dalton Trans.* **1980**, 383. (c) Hayward, C. M. T.; Shapley, J. *Inorg. Chem*. **1982**, *21*, 3816.

(18) (a) Earley, J. E.; Fealey, T. *J. Chem. Soc., Chem. Commun*. **1971**, 331. (b) Stanko, J. A.; Stanishak, T. W. *Inorg. Chem*. **1969**, *8*, 2156.

(19) (a) Teo, B. K. *J. Am. Chem. Soc*. **1981**, *103*, 3390. (b) Teo, B. K. *EXAFS: Basic Principles and Data Analysis;* Springer: Berlin, 1986.

(20) Jackson, P. F.; Johnson, B. F. G.; Lewis, J.; Mcpartlin, M.; Nelson, W. J. H. *J. Chem. Soc., Chem. Commun*. **1979**, 735.

(21) Goodwin, Jr. J. G.; Naccache, C. *J. Mol. Catal*. **1982**, *14*, 259.

(22) Niemantsverdriet, J. W.; van Langeveld, A. D. *Catalysis* **1987**, 769.

(23) Goodman, D. W.; Kelley, R. D.; Madey, T. E.; Yates, Jr., Y. T. *J. Catal*. **1980**, *63*, 226.

(24) Georeg, M. P.; Avery, N. R.; Weinberg. W. H.; Tebbe, F. N. *J. Am. Chem. Soc.* **1983**, *105*, 1393.

(25) (a) Demuth, J. E.; Ibach, H. *Surf. Sci*. **1978**, *78*, 1238. (b) Oxton, I. A.; Powell, D. B.; Sheppard, N.; Burgess, K.; Johnson, B. F. G.; Lewis, *J. Chem. Soc., Chem. Commun*. **1982**, 719.

(26) Shriver, D. F. *J. Organomet. Chem*. **1975**, *94*, 259.

(27) Lamb, H. H.; Gates, B. C.; Knozinger, H. *Angew. Chem., Int. Ed. Engl*. **1988**, *27*, 1127.

(28) Knox, S. A. R.; Koepke, J. W.; Andrews, M. A.; Kaesz, H. D. *J. Am. Chem. Soc*. **1975**, *97*, 3942.

(29) Zanderighi, G. M.; Dossi, C.; Ugo, R.; Psaro, R.; Theolier, A.; Choplin, A.; D′Ornelas, L.; Basset, J. M. *J. Organomet. Chem*. **1985**, *296*, 127.

(30) Goodwin, Jr., J. G.; Naccache, C. *J. Mol. Catal*. **1982**, *14*, 259.

(31) Hoffmann, R.; Schilling, B. E. R.; Bau, R.; Kaesz, H. D.; Mingos, D. M. P. *J. Am. Chem. Soc*. **1978**, *100*, 6088.

(32) Elian, M.; Hoffmann, R. *Inorg. Chem*. **1975**, *14*, 1058.

(33) (a) Green, J. C.; Seddon, E. A.; Mingos, D. M. P. *J. Chem. Soc., Chem. Commun*. **1979**, 94. (b) Green, J. C.; Mingos, D. M. P.; Seddon, E. A. *Inorg. Chem*. **1981**, *20*, 2595.

(34) van Zon, J. B. A. D.; Koningsberger, D. C.; van't Blik, H. F. J.; Sayers, D. E. *J. Chem. Phys*. **1985**, *12*, 5742.

(35) Wasowics, T.; Mickalik, J. *Radiat. Phys. Chem*. **1991**, *37*, 427.

(36) Shen, G. C.; Liu, A.-M.; Ichikawa, M. *J. Chem. Soc., Faraday Trans*. **1998**, *94* (9), 1353.

(37) Ito, T.; Wang, J.-X.; Lin, C. H.; Lunsford, J. H. *J. Am. Chem. Soc.* **1985**, *107*, 5062.

(38) Ashcroft, A. T.; Cheetham, A. K.; Foord, J. S.; Green, M. L. H.; Grey, C. P.; Murrell, A. J.; Vernon, P. D. F. *Nature* **1990**, *344*, 319.

(39) Shelimov, B. N.; Kazansky, V. B. *J. Chem. Soc., Faraday Trans*. **1987**, *83*, 2381.

(40) Belgued, M.; Monteverdi, S.; Pareja, P.; Amariglio, H. Amariglio, A.; Saint-Just, J. Symposium on Natural Gas Upgrading II, American Chemical Society, San Francisco Meeting, Apr 5−10, 1992.

(41) Koerts, T.; van Santen, R. A. *J. Chem. Soc., Chem. Commun*. **1991**, 1281.

(42) Koerts, T.; van Santen, R. A. *Catal. Lett*. **1990**, *6*, 49.

(43) Yang, H.; Whitten, J. L. *Surf. Sci*. **1991**, *255*, 193.

(44) Shriver, D. F. *J. Organoment. Chem*. **1975**, *94*, 259.

(45) Miller, J. T.; Modica, F. S.; Meyers, B. L.; Koningsberger, D. C. *Prepr., Div. Petrol. Chem., Am. Chem. Soc*. **1993**, *38*, 825.

(46) van Zon, J. B. A. D.; Koningsberger, D. C.; van't Blik, H. F. J.; Sayers, D. E. *J. Chem. Phys*. **1985**, *12*, 5742.

(47) Kosugi, N.; Kuroda, H. *Program EXAFS 2*, Research Center for Spectrochemistry, University of Tokyo, 1988.